Programmable Non-Epipolar Indirect Light Transport: Capture and Analysis

Hiroyuki Kubo ⓘ, Suren Jayasuriya ⓘ, *Member, IEEE*, Takafumi Iwaguchi,
Takuya Funatomi ⓘ, *Member, IEEE*, Yasuhiro Mukaigawa ⓘ, *Member, IEEE*,
and Srinivasa G. Narasimhan ⓘ, *Senior Member, IEEE*

Abstract—The decomposition of light transport into direct and global components, diffuse and specular interreflections, and subsurface scattering allows for new visualizations of light in everyday scenes. In particular, indirect light contains a myriad of information about the complex appearance of materials useful for computer vision and inverse rendering applications. In this paper, we present a new imaging technique that captures and analyzes components of indirect light via light transport using a synchronized projector-camera system. The rectified system illuminates the scene with epipolar planes corresponding to projector rows, and we vary two key parameters to capture plane-to-ray light transport between projector row and camera pixel: (1) the offset between projector row and camera row in the rolling shutter (implemented as synchronization delay), and (2) the exposure of the camera row. We describe how this synchronized rolling shutter performs illumination multiplexing, and develop a nonlinear optimization algorithm to demultiplex the resulting 3D light transport operator. Using our system, we are able to capture live short and long-range non-epipolar indirect light transport, disambiguate subsurface scattering, diffuse and specular interreflections, and distinguish materials according to their subsurface scattering properties. In particular, we show the utility of indirect imaging for capturing and analyzing the hidden structure of veins in human skin.

Index Terms—Light transport, indirect light, synchronized projector-camera system, computational photography

---◆---

1 INTRODUCTION

LIGHT transport describes the transfer of radiant energy in a scene between illumination sources and detectors. Light can follow a direct path from illumination source to scene object to camera or undergo multiple, indirect bounces in the scene, and all these paths contribute to the final image captured by the camera. Selective capture of these different light transport components has many useful applications in computer graphics and vision. Direct light allows for accurate estimation of depth and surface normals for structured light, time-of-flight, active and photometric stereo [1], [2], [3]. Knowledge of indirect light can perform inverse rendering for subsurface scattering materials such as wax and human skin [4]. Emerging applications utilize

• *H. Kubo is with the Nara Institute of Science and Technology, Ikoma, Nara 630-0192, Japan, and also with Carnegie Mellon University, Pittsburgh, PA 15213 USA. E-mail: hkubo@is.naist.jp.*
• *S. Jayasuriya is with the School of Arts, Media, and Engineering and the School of Electrical, Computer, and Energy Engineering, Arizona State University, Tempe, AZ 85281 USA. E-mail: sjayasur@asu.edu.*
• *T. Iwaguchi is with the Nara Institute of Science and Technology, Ikoma, Nara 630-0192, Japan, Carnegie Mellon University, Pittsburgh, PA 15213 USA, and also with Kyushu University, Fukuoka 819-0395, Japan. E-mail: iwaguchi@ait.kyushu-u.ac.jp.*
• *T. Funatomi and Y. Mukaigawa are with the Nara Institute of Science and Technology, Ikoma, Nara 630-0192, Japan. E-mail: {funatomi, mukaigawa}@is.naist.jp.*
• *S.G. Narasimhan is with the Robotics Institute, Carnegie Mellon University, Pittsburgh, PA 15213 USA. E-mail: srinivas@cs.cmu.edu.*

multi-bounce indirect light to image objects outside the line-of-sight of the camera [5].

One particular application of interest for this paper is using indirect light to visualize the hidden structure of blood vessels in human skin. Skin features strong subsurface scattering that reduces the contrast necessary to image these features. By capturing indirect light, one can enhance the signal-to-noise ratio for the blood vessels of interest. This has numerous biomedical and clinical applications including helping physicians and nurses locate blood vessels for injections and surgical procedures. This skin imaging should be non-destructive, perform in both indoor and outdoor environments, and not require expensive or high-powered technology.

Acquisition of the full light transport in a scene typically requires a prohibitively large number of images. To alleviate this, imaging methods to selectively capture light transport components efficiently have been invented. These include direct-global separation [6], and short and long-range indirect light separation via primal-dual imaging [7], [8]. Recent work has linked light transport to the epipolar geometry of projector-camera systems [8], [9]. In this formulation, *epipolar light* is defined as light paths on the same epipolar plane aligned with the rows of a rectified projector-camera system, and *non-epipolar light* is all the indirect light paths not on the same epipolar plane.

In this paper, we further explore the relationship between epipolar geometry of a projector-camera system and light transport, particularly for *indirect light transport*. By doing so, we show how this system can acquire indirect light transport, and that it has varied applications in
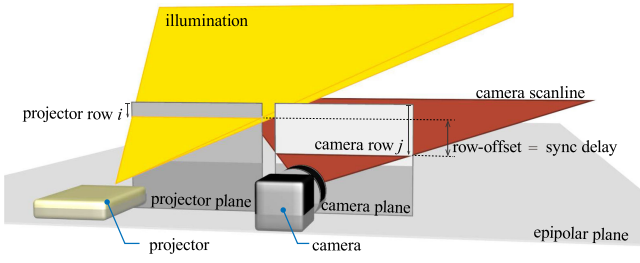
Fig. 1. A rectified projector-camera system to implement plane-to-ray light transport. The laser projector illuminates the scene with a plane that is swept vertically. The camera synchronizes its rolling shutter to a fixed row-offset from the illumination plane. As each projector row advances, so does the exposed camera row. By varying both the delay between synced camera and projector rows as well as the camera row exposure, we can capture live various components of epipolar and non-epipolar light transport.

computational relighting and material recognition. In particular, we demonstrate that this imaging system is a robust platform for real-time imaging of blood vessels in human skin with excellent contrast visibility and resilience to ambient illumination.

Our imaging technique exploits the light transport between the projector's epipolar planes of illumination and camera pixels for capturing and analyzing non-epipolar indirect light paths. In our system, a projector illuminates a plane of light corresponding to a projector row as shown in Fig. 1. This light is captured by exposed rows of the camera's rolling shutter. Since the camera and projector are rectified in an epipolar configuration, the difference between epipolar and non-epipolar light paths is determined by the vertical separation between projector and camera rows shown in Fig. 1. By controlling light transport from illumination plane to camera ray, we can selectively acquire these non-epipolar indirect light paths.

Each camera ray is determined by the transport of 1D planar illumination from the projector to a 2D pixel. We observe that a rolling shutter camera, synchronized to the projector and in an epipolar configuration, performs illumination multiplexing of this transport using the parameters of (1) *synchronization delay or row offset* between the illuminated projector row and exposed camera row, and (2) *exposure* of the camera row itself. Throughout this paper, we refer to synchronization delay or row offset interchangeably. Note that this delay is not equivalent to the temporal delay commonly used in transient imaging.

In our new imaging technique, we capture image stacks of varying sync delay and exposure to analyze and capture different light transport paths in the scene. In particular, we make the following contributions:

- Capture of short and long-range non-epipolar indirect light in real-time with our system.
- Modeling and analysis of the illumination multiplexing performed by the synchronized rolling shutter.
- A nonlinear optimization algorithm to demultiplex this illumination and recover 3D light transport between the projector and camera.
- Analysis of delay profiles for subsurface scattering, diffuse and specular interreflections.
- Enhanced skin imaging including real-time visualization, robustness to ambient light, and algorithms

for contrast-enhancement and improved pulse extraction using motion magnification on non-epipolar indirect light.

We demonstrate applications including sharpened (coarse-to-fine) epipolar imaging, subsurface scattering material recognition, and real-time vein visualization in human skin. We validate our ideas on real experimental data from the epipolar imaging system Episcan3D (the system was first presented in Section 5 of [8]). This research allows for parametric control for these active illumination systems through the knobs of sync delay and exposure. This enables even more selectivity of the light transport paths we probe and capture.

A preliminary version of this paper appeared at the International Conference on Computational Photography (ICCP) 2018 [10]. This paper extends the conference version in Section 5 via analyzing our illumination demultiplexing algorithm including its performance for a subsurface scattering model, as well as presenting extensive new results for skin imaging in Section 10. These new results include (1) real-time imaging of non-epipolar indirect light from blood vessels in skin, including comparison to a state-of-the-art medical imaging device under strong ambient light conditions, (2) an algorithm to enhance the contrast for skin imaging, and (3) motion magnification to extract blood pulse from these vessels.

2 BACKGROUND AND RELATED WORK

Light transport matrices [11], [12], [13] model the linear relationship between illumination sources and detectors. Given P light sources represented with vector $\vec{p}$, and N detectors represented by vector $\vec{i}$, a light transport matrix T is a $N \times P$ matrix satisfying: $\vec{i} = T\vec{p}$. Each element $T[a, b]$ describes the ratio of radiant energy sent through a set of light paths from light source b to detector pixel a. Efficient acquisition for light transport matrices includes compressive sensing at reduced measurements [14], [15], approximation via symmetry [16], and optical computing via matrix-vector products [17]. Methods have also decomposed light transport into bounces of light [18] and its subcomponents of light [19].

There also has been much interest in acquiring specific components or slices of the light transport matrix directly using imaging systems. The seminal work by Nayar et al. [6] showed that direct light whose light paths bounce only once in a scene between illumination source and detector could be separated from global light whose light paths bounce more than once in the scene. Global light is the sum of indirect light components, including short and long range indirect light. The separation was achieved by projecting high spatial frequency illumination patterns (e.g., a checkerboard pattern), and then performing a per-pixel equation to calculate direct and global images. A minimum of 2 images is theoretically required, but in practice tens of images are utilized for robust performance. This separation could be shown even for subsurface scattering materials with a high spatial frequency. Further research extended direct-global separation to account for motion compensation [20] and multiple light sources [21], and primal-dual coding has been used to enable live video separation [7], [9].

Beyond direct/global separation, researchers have explored even finer-grained decompositions of light transport. Global light has been decomposed further into short and long-range indirect light, corresponding to effects such as subsurface scattering (short) and diffuse interreflections (long). Reddy et al. used frequency analysis of spatially varying illumination to capture short and long-range indirect light [22] while O'Toole et al. utilized homogeneous codes for a primal-dual imaging system [8] to capture these effects in a single exposure. In addition, diffuse and specular reflections have been separated using color and polarization cues [23], [24], [25], [26]. Diffuse light transport has been partially decomposed while keeping consistent interreflections in the scene [27]. Similar to our paper but with time-resolved measurements, Wu et al. used temporal delay profiles to analyze indirect light transport and material properties [28].

Multiplexed Illumination and Exposure. One fundamental limitation for capturing finer-grained components of light transport is the low signal-to-noise (SNR) ratio of detectors with low light. To solve this issue, most imaging schemes utilize illumination multiplexing where multiple light sources are turned on, and then later decoded into their individual contribution in post-processing. This effectively boosts the SNR at acquisition time due to more light. For general illumination multiplexing, it has been shown that Hadamard codes maximize SNR with respect to a generic signal-independent noise model [29], and further optimal codes can be derived when considering realistic Poisson-distributed photon noise and sensor saturation [30].

Several methods have been introduced to multiplex illumination for light transport acquisition. Sen et al. use an adaptive light multiplexing algorithm to efficiently capture light transport matrices [31]. On the camera side, coded exposure methods enable motion deblurring [32], video from a single coded exposure [33], rolling shutter photography [34], and space-time voxels [35].

Imaging Systems for Light Transport Acquisition. The light stage uses a large installation of light sources and cameras to acquire light transport for human subjects [11], [36], [37], [38], [39]. At a smaller scale, several smaller prototype systems have been created including regular projector-camera systems [31], coded exposure [33], [35], and primal-dual coding via digital micromirror devices [7]. Researchers have acquired light transport for translucent materials using a scanning laser over rotated samples [40]. For temporally synced projector-camera systems, researchers have modified DLP projectors for fast projection [41].

Imaging Systems for Skin Imaging. There have been recent advances to visualize blood vessels using infrared wavelengths which penetrate skin deeper than visible light [42] and active illumination techniques including Laser Speckle Contrast Imaging (LSCI) [43] and Sidestream Dark Field (SDF) Imaging [44]. Direct/global separation has also been applied for enhancing contrast for visualizing blood vessels and flow [45], [46]. Facial reflectance has been captured by modeling light scattering in skin [47]. In addition, there has been several works on extracting blood pulse using photoplethysmography (PPG) [48], [49] as well as motion magnification [50]. In this paper, we show that indirect light capture using our imaging system can also

reveal the inner structure of blood vessels in human skin in real-time capture.

Epipolar Imaging and Light Transport. The work most similar to ours is O'Toole et al. [8] who specified the epipolar geometry of a rectified projector-camera system. In Fig. 1, the projector and camera are rectified so that their rows are aligned on the same epipolar plane. Intuitively, this divides the scene into a stack of epipolar planes, each of which contains the epipolar line connecting the projector and camera centers as well as a unique projector/camera row.

The relationship between light transport and epipolar geometry is determined by this alignment [8], [9]. Direct light, which must lie on the same epipolar plane since it is defined by the intersection of the projector and camera rays, can only travel from projector row i to the same camera row i. Indirect light, which has undergone multiple bounces, can travel from projector row i to any camera row j. However, the amount of indirect light on the epipolar plane, light that has undergone multiple bounces but still travels from projector row i to camera row i, is a small percentage of the total indirect light (unless there are strong specular interreflections in the scene).

O'Toole et al. [8] invented Episcan3D as a hardware implementation of epipolar imaging. Episcan3D is also the main hardware platform we utilize in this paper. Episcan3D uses the syncing between a laser projector and the rolling shutter of a camera to selectively capture epipolar light when the rolling shutter only exposes camera rows on the same plane as the illuminated projector row, and non-epipolar light when the rolling shutter exposes all camera rows except the row on the same plane as the illuminated projector row [8]. This decomposition of epipolar and non-epipolar light is done in real-time. Epipolar imaging was later extended to a time-of-flight device to obtain more accurate depth measurements and robustness to ambient light [3].

We note that the synchronization of the camera's rolling shutter to a raster-scanning projector to capture epipolar and non-epipolar light is the contribution of [8]. However, the insight that this mechanism can be interpreted as illumination multiplexing, and we can utilize delay-exposure stacks to demultiplex and recover 3D light transport is novel to this paper. Further, we show new applications of epipolar imaging including epipolar sharpening, synthetic 1D relighting, enhanced direct/global separation, material recognition for subsurface scattering, and real-time blood vessel imaging in human skin.

3 PLANE-TO-RAY LIGHT TRANSPORT

In this section, we describe the principles of our imaging modality. We first exposit planar illumination and its light transport. We then show how light multiplexing occurs using the delay and exposure of a temporally-synced projector and rolling shutter camera system. We derive expressions for these parameters, and use them to model the illumination function and image stack formation.

As stated in the previous section, we follow the formulation of O'Toole et al. [8] for epipolar geometry of a projector-camera system and light transport. Epipolar imaging captures light paths that travel from projector row i to rectified camera row i. Non-epipolar imaging captures indirect

light traveling from projector row i to any camera row $j \neq i$. Thus, the planar light transport from projector to camera is parameterized by the relative offset between projector row i and camera row j, and controlled by the *synchronization delay*, the timing difference between the synchronized projector scanning and camera rolling shutter. In addition, the *exposure* of the camera row determines the amount of integrated light at each camera row. The light transport operator describes the transfer of radiant energy from projector row to camera pixel, hence we title this plane-to-ray light transport.

In an ideal planar illumination system, one could capture the light transport by projecting one line at a time and taking an image. However, this impulse scanning suffers from low SNR due to low light levels [29], especially for subsurface scattering and long-range indirect light. In addition, in a real system, the laser itself has a temporal jitter, which may cause light to leak into neighboring rows as noticed in [8]. To solve these issues, we use the key insight that the rolling shutter, synchronized to the projector, performs light multiplexing of this planar illumination. This light multiplexing increases the SNR for light transport acquisition. Thus we describe this light multiplexing using the parameters of delay and exposure in a rolling shutter system, and propose an algorithm to demultiplex and recover the 3D light transport in the subsequent section.

3.1 Light Multiplexing Using Delay and Exposure

For a rolling shutter camera synchronized to the epipolar illumination of the projector, we can control the delay and exposure of this shutter to perform light multiplexing. The exposure determines the number of rows being exposed with larger exposures leading to larger sets of rows being exposed. The delay is the distance between the illuminated projector row and the center of the exposed rows.

The rolling shutter of the camera can be synchronized to the projector illumination, as described in [8]. In particular, this means the pixel clock is fixed and focal length of the lens adjusted so that the projector rows and camera rows change with the same vertical velocity. In epipolar imaging mode, the delay is zero, so that the band of exposed camera rows is on the same epipolar plane as the light being projected, while in non-epipolar mode, the band of exposed camera rows does not include the epipolar plane where the light is. Light multiplexing occurs since each row gets light from multiple projector lines due to the width of the exposure and the value of the delay. To describe the demultiplexing algorithm in Section 4 necessary to estimate 3D light transport, we first must derive the relationship between delay and exposure, and use it to model the illumination.

Relationship Between Delay and Exposure. We use the same notation as [8] to parametrize delay and exposure in a rolling shutter system. Let t_p denote the amount of time for which the projector illuminates a single scanline (with some finite band width), t_e be the exposure time which corresponds to a contiguous block of rows being exposed, and t_o denote the time offset of synchronization between the projector and camera. Additionally, we denote t'_o as the time difference between the start of exposure and when the projector illuminates that row of pixels. Please see Fig. 3 for a visual description of these parameters.

As we change t_o, this changes t'_o, and thus we express delay: t_d as the difference between the center times of exposure and illumination, as following:

$$t_d = \frac{1}{2}t_e - \frac{1}{2}t_p - t'_o. \tag{1}$$

Positive $t_d > t_e/2$ means the camera row receives light from a vertically lower epipolar plane. Similarly, negative $t_d < -t_e/2$ means the light arrives from a vertically higher epipolar plane. If $0 \leq |t_d| \leq t_e/2$, then the exposed row receives a majority of illuminated light from the same epipolar plane. Typically, epipolar imaging operates with $t_d = 0$ and t_e as short as possible (as shown in Fig. 3c).

Illumination Model. We formulate a model for the illumination as a function of delay and exposure. Using calibration, we obtain the speed of the projector scanline v_p sec/line in the scene. Given this, we express illumination band width I_w and its center location I_d by the following equations:

$$I_w(t_e) = v_p t_e, \qquad I_d(t_d) = v_p t_d. \tag{2}$$

Let v denote a row of the projector plane. We then define the illumination function $L(v, t_d, t_e)$

$$L(v, t_d, t_e) = \begin{cases} 1, & \text{if } \|v - I_d(t_d)\| < \frac{1}{2}I_w(t_e); \\ 0, & \text{otherwise} \end{cases}. \tag{3}$$

Note that we define the maximum intensity of the projector as 1. We will use this illumination function to estimate 3D light transport amongst rows of the projector/camera in Section 4.

4 3D LIGHT TRANSPORT ESTIMATION VIA DEMULTIPLEXING

In the previous section, we formulated the light multiplexing caused by the rolling shutter parameterized by delay and exposure. We now develop a demultiplexing algorithm to estimate the plane-to-ray light transport.

Delay-Exposure Image Stacks. We first capture a series of images while varying delay t_d and exposure t_e. We typically use uniformly sampled points between minimum and maximum values for both delay and exposure as part of our sweep.

By controlling the delay and exposure, we have the ability to capture short and long-range non-epipolar light. As the delay increases, light from the illumination plane has to travel a longer vertical distance to reach the camera row. This gives a minimum bound of the optical path length traveled by the indirect light. By controlling the exposure, we can allow more or less amount of light that has traveled this minimum bound, thus creating a *band* of non-epipolar light. This corresponds to banded diagonals off the main diagonal in a light transport matrix [8], [9]. In Section 7 we demonstrate results of this banded imaging.

Optimization. For given t_d and t_e, the observation I at pixel (s, t) is given by the product of the illumination with the light transport operator, integrated over the projector rows v, to form the final image

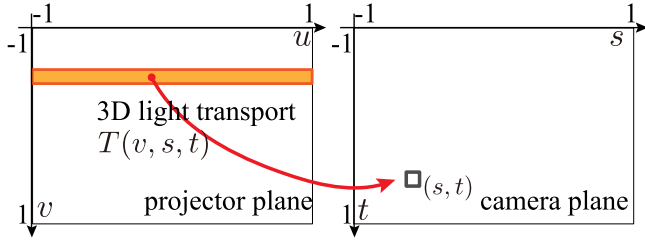$$I(s, t) = \int L(v, t_d, t_e) T(v, s, t) dv. \tag{4}$$

Fig. 2. Illustration of plane-to-ray 3D light transport $T(v, s, t)$ from row v in projector plane to a camera pixel (s, t).

Note that, $T(v, s, t)$ is 3D light transport from row v to a pixel(s, t). This relationship is illustrated in Fig. 2. We note that this equation can be discretized to the standard matrix-vector product of light transport.

We can write the epipolar and non-epipolar images by the following equations:

$$I_e(s, t) = \int \delta(t - v) T(v, s, t) dv, \tag{5}$$

$$I_n(s, t) = \int (1 - \delta(t - v)) T(v, s, t) dv. \tag{6}$$

Hence, if we can estimate T from the image stack of varying t_d and t_e, we can synthesize epipolar and non-epipolar images. We denote the i-th image with delay $t_{d,i}$ and exposure $t_{e,i}$. Thus we estimate the light transport T^* as the solution to the following optimization problem:

$$\underset{T(v,s,t)}{\operatorname{argmin}} \sum_i^N \left\| I_i - \int L(v, t_{d,i}, t_{e,i}) T(v, s, t) dv \right\|_2^2 + \alpha E_c + \beta E_s,$$

$$\text{subject to } T \geq 0, \ \forall v, \quad E_c = \left\| \frac{\partial}{\partial v} T \right\|_2^2, \quad E_s = \|T\|_1.$$

We use additional regularization for smoothness and sparsity in the light transport: α and β are coefficients of smoothness and sparsity respectively. This helps with the optimization to reduce noise and other image artifacts. The total number of images in the stack is N. In practice, we utilize $\alpha = 0.01$, $\beta = 0.01$, and $N = 75$.

Since the formulation is per-pixel, the optimization is easily parallelizable. We use the CVXPY framework for convex optimization to solve this [51]. We feed most delay-exposure images to the solver except for those delay images which lie on the boundary between epipolar and non-epipolar imaging ($t_d \approx t_e/2$), which have significant horizontal artifacts due to synchronization problems.

The main limitations of our algorithm is the enforcement of smoothness and sparsity conditions on the light transport we recover. This prevents us from recovering very small intensity visual effects (as the sparsity condition will drive these light paths to zero) or handling long-range indirect light paths due to the smoothness condition on the light transport. However, without these regularization terms, the optimization algorithm does not converge to a meaningful light transport operator as the inverse problem is under-determined and requires constraints to help solve this.
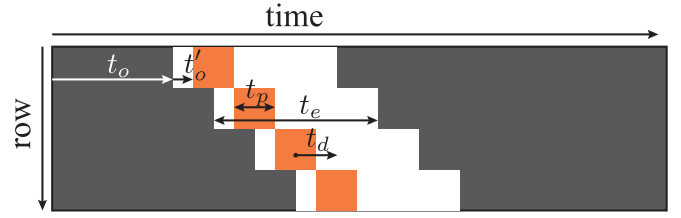
(a) The projector illuminates a single row for a time t_p in orange. At the same time, the rolling shutter exposes a single row for length t_e. Light from a single row (orange) will be captured not just by the same camera row, but rows above and below it that are being exposed (white). Delay t_d is the distance from center of exposure to the center of illumination. t'_o is the time between start of exposure and illumination in a row, and t_o is the synchronization offset from projector to camera.
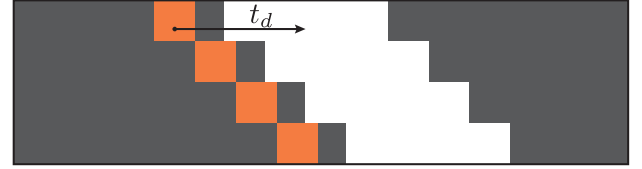
(b) As the delay is increased, the illuminated projector row sends light to camera rows that are at least one row above it. This corresponds to short range non-epipolar light paths in the scene.
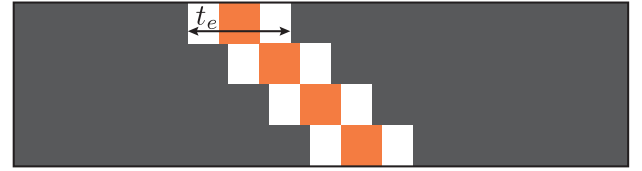
(c) As the exposure is decreased, the illuminated projector row leaks less light into neighboring rows, resulting in a majority of epipolar light paths captured.

Fig. 3. Timing diagram of projector illumination and camera rolling shutter for epipolar imaging.

5 ANALYSIS OF ILLUMINATION DEMULTIPLEXING

In this section, we analyze the performance of our illumination demultiplexing algorithm. We first compare and contrast between our multiplexed illumination strategy which requires an epipolar (synced and aligned) projector-camera versus more traditional projector-camera algorithms via spatially-varied lighting. We then simulate the performance of our optimization algorithm with respect to noise for recovering subsurface scattering profiles, and empirically validate the choice of regularization and constraints in our optimization.

5.1 Comparison to Traditional Projector-Camera Systems

A traditional projector-camera system can perform direct-global separation as shown in [6]. Thus it is natural to ask how an epipolar projector-camera system can be more advantageous for illumination demultiplexing. An epipolar system requires two additional setup complexities: (1) the need for epipolar rectification via optical alignment and (2) synchronization for controlling the exposure/delay. We analyze both of these conditions and their trade-off with respect to conventional projector-camera acquisition.

While direct-global separation can be performed digitally with a traditional projector-camera system, epipolar/non-epipolar separation is only possible by optically aligning the projector and camera to be rectified [8]. Epipolar separation has more robust performance on specular and shiny

(a) Scene   (b) 720 images   (c) Direct image without sync   (d) Direct image with sync
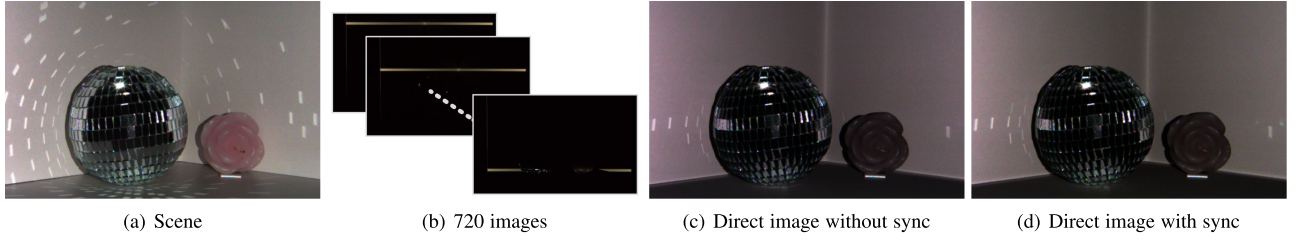
Fig. 4. Comparison between an optically rectified projector-camera system with and without synchronization. Note that by illuminating one row at a time as shown in (b) and digitally extracting pixel rows in post-processing, we can create qualitatively similar results for selective light transport capture. However, synchronization allows for real-time imaging for epipolar and non-epipolar light components that is not possible using digital post-processing methods.

materials, which are challenging for conventional direct-global separation with its frequency assumptions [6]. Once a projector-camera is optically rectified, it is possible to digitally perform our method of illumination multiplexing to capture epipolar and non-epipolar images. We project a horizontal band of light of a certain width into the scene, and only a certain row of pixels offset a distance away from this illumination bar (delay t_d) would be extracted and retained. We then shift this horizontal illumination one row down, and extract the next row of pixels from the previous row extracted. By sweeping this illumination with multiple images, we can synthesize a single image of fixed delay t_d. This mimics the epipolar illumination configuration used in Episcan3D in post-processing. In Fig. 4, we implement this method, and compare the direct images with and without synchronization. Note that the images look qualitatively similar, although the direct image without synchronization has slightly softer highlights for the reflections and some color difference as compared to synchronization.

The advantage of this digital illumination method is that it allows exposure to be decoupled from acquiring delay images, which could boost signal for very low light images. However, the main caveat is that multiple images must be acquired to form a single delay image if the system is not sychronized. Synchronization allows for real-time selective light transport imaging such as epipolar, non-epipolar imaging and the delay imaging for skin-visualization shown in Section 10. We do note that spatial multiplexing of these illumination patterns could reduce this acquisition cost, especially since our demultiplexing algorithm does not consider long-range indirect light effects. This is an interesting avenue of future work to determine the trade-offs between spatial illumination multiplexing, setup complexity, and exposure/delay control for epipolar systems.

5.2 Demultiplexing Performance

To validate the performance of our illumination demultiplexing, we perform simulations where we recover the light transport for a subsurface scattering model. We simulate our forward imaging equation with an additive noise model

$$I(s,t) = \int L(v, t_d, t_e)T(v, s, t)dv + \eta,$$

where noise η is normally distributed with zero mean. For our simulations, we illuminate a single pixel in the center (the projector is orthogonal to the material surface), and measure the scattering profile in a column of camera pixels

using a Monte Carlo simulation. This 1D scattering profile is then used to simulate illumination multiplexing, which we then recover via our demultiplexing algorithm.

For light transport $T(v)$ at a pixel, we utilize a subsurface scattering model for layered surfaces that is simplified to one-dimensional light transport theory [52]. This model assumes the object is comprised of homogeneous participating media parameterized by absorption coefficient σ_a, scattering coefficient σ_s, and Henyey-Greenstein phase function

$$p(\theta) = \frac{1}{4\pi} \frac{1 - g^2}{\left(1 + g^2 - 2g\cos\theta\right)^{3/2}},$$

where θ is the angle between incident and outgoing light, and g is the mean cosine for the scattered light. Note that $g = 0$ gives isotropic scattering, $g > 0$ is forward scattering, and $g < 0$ is back scattering. We use the bidirectional path tracing algorithm to render the material in the Mitsuba renderer [53].

We note to the reader that this is a simplified model for subsurface scattering, and that more advanced BSSRDFs that take into account incident direction [54] or more complex scattering [55] can be considered. However, we felt this model had sufficient complexity for the forward scattering materials we consider, and to show evidence that the demultiplexing can recover light transport. In Section 8, we validate that our method works on real subsurface scattering materials including milk, soap, and toothpaste.

Since our illumination demultiplexing algorithm is novel due to the configuration of our imaging system, there are no direct related work or competing methods from the literature to perform the demultiplexing. Instead, we compare against standard optimization techniques including the pseudo-inverse and a least-squares with non-negative constraint $T \geq 0$. In Fig. 5a, we reconstruct the light transport of the scattering material comparing standard optimization techniques against our least-squares with non-negative constraints and regularization as formulated in Section 4. Note how the pseudo-inverse yields negative values for the estimated light transport, and thus motivated the need for non-negative constraints. The addition of regularization terms helped improve the performance of the optimization algorithm. In Fig. 5b, we simulate the performance of these different reconstruction techniques as we increase the strength of the noise. While the pseudo-inverse can sometimes yield lower MSE than our full optimization with regularization (especially at low noise levels), it should be noted that its solution is incorrect due to the presence of negative values.
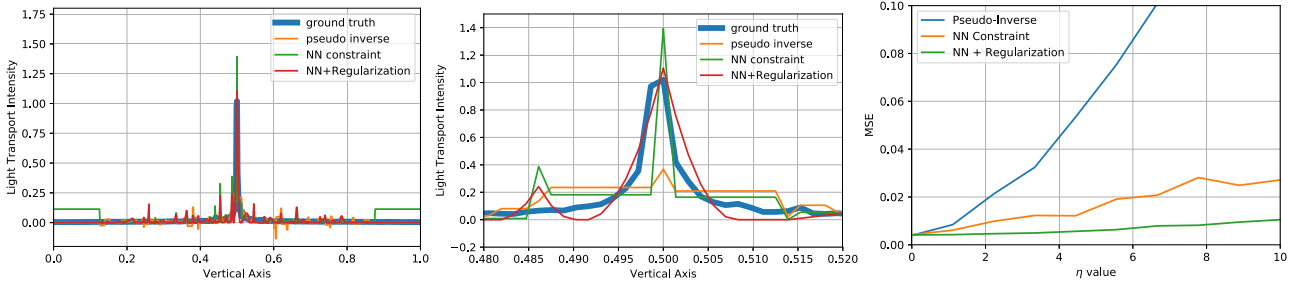
Fig. 5. (a) Result of reconstruction algorithms for a simulated T modeled by subsurface scattering with Henyey-Greenstein phase function [52], with a close-up of the peak in (b). (c) Performance of reconstruction algorithms for different noise levels η. All simulations use $\sigma_s = 1, \sigma_a = 0, g = 0.9$, $\eta = 0.05$ when a parameter is not being swept as their default configuration.

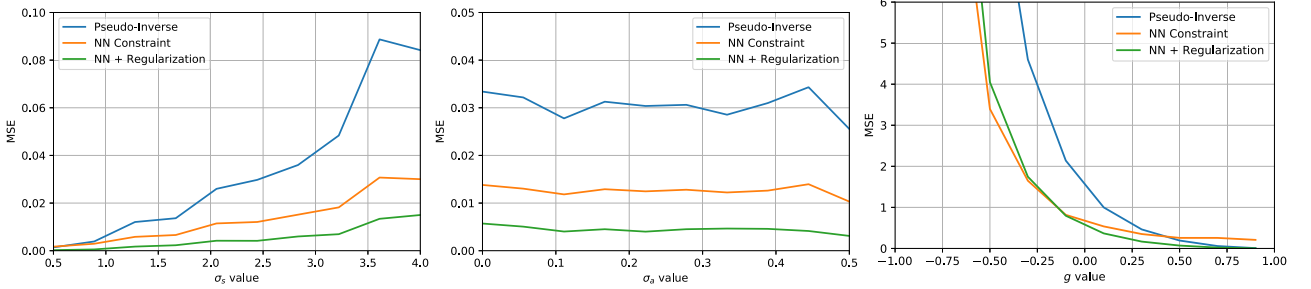Fig. 6. (a) MSE as the scattering coefficient σ'_s changes, (b) MSE with respect to the absorption coefficient σ_a (c) MSE for differing values of g in the phase function. All simulations use $\sigma_s = 1, \sigma_a = 0, g = 0.9, \eta = 0.05$ when a parameter is not being swept as their default configuration.

At high noise levels, our least squares with non-negative constraint and regularization performs the best.

In Fig. 6, we show reconstruction performance as a function of the scattering, absorption, and g coefficients. Note that for scattering and absorption coefficients in a strongly forward scattering regime $g = 0.9$, our method performs better than methods without regularization. Fig. 6b corresponds to making the material darker as the absorption increases, as all other tests are performed with white materials of absorption zero. For g, our method performs better for $g > 0$, and starts to perform worse for $g < -0.25$ backscattering. However, we note that most materials of interest we consider such as milk are forward scattering [56], and thus our method works well for these materials (also verified in our experimental results in Section 8).

6 HARDWARE IMPLEMENTATION

To implement our ideas, we utilize the Episcan3D system described in [8]. We also discuss calibration and acquisition process for capturing delay-exposure image stacks.

Prototype. We utilize similar prototypes to the Episcan system [8] and shown in Fig. 7. We use a Celluon PicoPro as a projector with display resolution 1280×720, and either an IDS UI-3250CP-C-HQ color camera or IDS UI-3250CP monochrome camera with both global and rolling shutter capabilities. The shutter is triggered by the VSYNC signal generated by the projector, and also can be delayed by the camera using t_o. We refer the reader to the supplemental material, which can be found on the Computer Society Digital Library at http://doi.ieeecomputersociety.org/10.1109/TVCG.2019.2946812, of [8] about the support circuitry and physical alignment required for the prototype.

Calibration. For our calibration procedure, it is necessary to determine the illumination bandwidth I_w and center

location I_d with respect to t_e. From Equation (2), we see that we need to estimate v_p. To do this, we project a single-pixel horizontal white line on a black background, and sweep the line vertically from top to bottom. We image this sweep in global shutter mode with $t_e = 500$ microseconds,. By counting the number of visible lines n_v, we obtain the projector scanline velocity $v_p = n_v/t_e$. Typically we observe 27 lines in 500 microseconds, exposure observation, so we calculate $v_p = 27/(500 \times 10^{-3}) = 54,000$ lines/sec.

Acquisition. To acquire images, we use 12 bit capture and average 8 images for each delay and exposure. We captured images without gamma correction, and verified that the resulting image measurements were linear by measuring the camera response curve. For a typical sweep, we used delay $t_d = -1500$ to 1500 microseconds with step size 187.5 microseconds, and exposure $t_e = 600$ -1200 microseconds with step size of 150 microseconds. The ability to control the rolling shutter's delay and exposure was given by the IDS software of the camera manufacturer through their API.
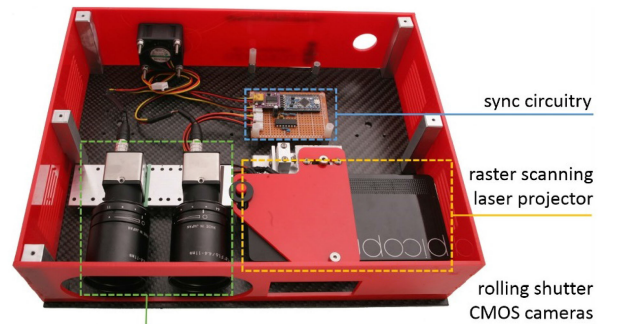

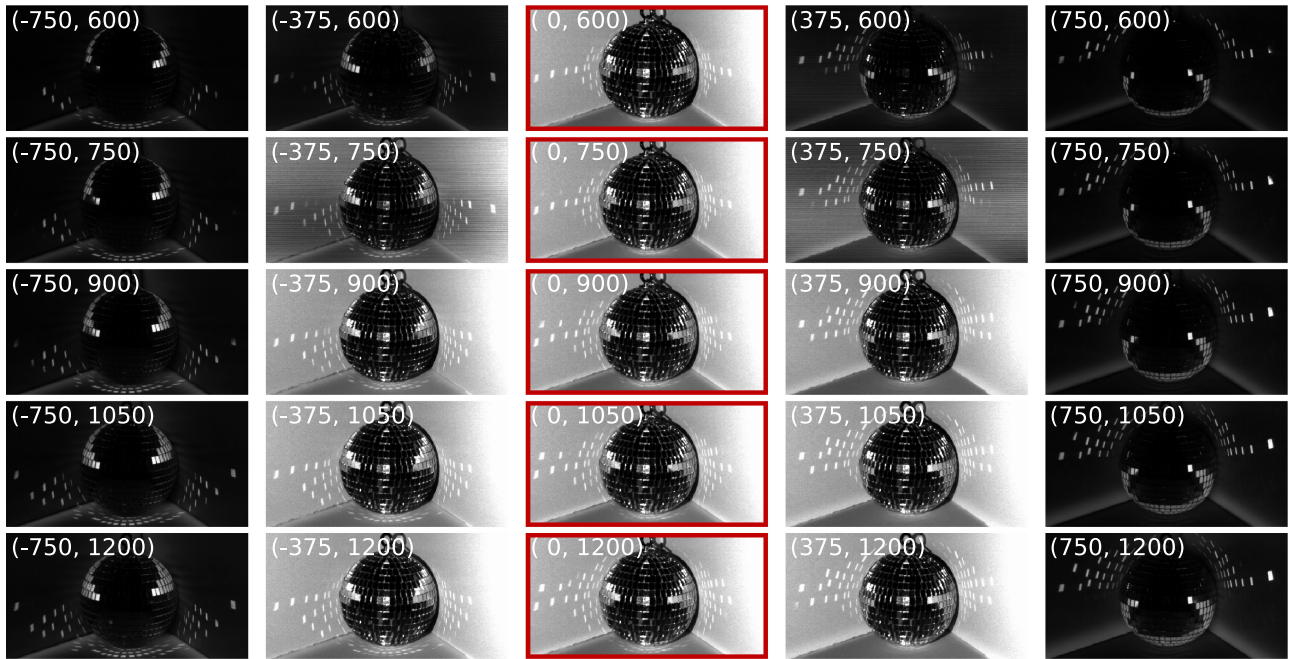Fig. 7. The Episcan3D prototype [8] which we use for our epipolar imaging system.

Fig. 8. An image stack of varying delay on the x-axis and exposure on the y-axis, with values (t_d, t_e) in microseconds. Epipolar images occur when $|t_d| < t_e/2$, and non-epipolar or indirect light otherwise, and are denoted by the red boxes. Notice how the specular interreflections of the disco ball move vertically as delay increases in one row corresponding to indirect light paths jumping from illumination to received plane. The size of the interreflections band is controlled by exposure. All images are equally brightened for visualization.

Total acquisition time is as follows: Calibration takes approximately 4 minutes (one-time only process), acquisition for 75 images (a typical delay-exposure stack) takes approximately 2 minutes where each image is an average of 8 frames, and it takes 9 minutes to demultiplex these images for 128×128 resolution.

7 RESULTS: DELAY-EXPOSURE IMAGING

As described earlier, controlling the delay and exposure can selectively image bands of non-epipolar indirect light in a scene. We captured several image stacks sweeping exposure and delay with uniform increments. In Fig. 8, we visualize the specular interreflections of a disco ball shifting vertically as the delay changes.

As you can see in cross-sections of Fig. 8, with $t_d = 0$ microseconds, mostly direct light is captured, but more indirect light leaks in as the exposure is increased from 600 microseconds, to 1,200 microseconds,. We note that this effect is particularly noticeable due to the brightness of specular interreflections of the disco ball, and other diffuse interreflections cannot have tight indirect bands due to low exposure. Please view a video of sweeping the band in the supplemental material, available online.

Noise is primarily determined by the amount of light reaching the pixels (although there are synchronization artifacts at very short exposure times due to jitter in the laser raster scan). For indirect imaging, specular interreflections (such as the disco-ball reflections) are brighter and thus less noisy than diffuse interreflection or subsurface scattering effects. Since exposure is coupled to the band of light received by the rolling shutter, there is a trade-off between integrating more light and the tightness of the band of indirect light (i.e., the resolution of the illumination function).

8 RESULTS: DELAY PROFILES AND MATERIAL RECOGNITION

Delay Profiles. For each pixel, we can plot the pixel intensity as a function of the delay t_d. We call this a *delay profile*, and it yields information about the scattering of light with respect to the planar illumination of the projector. Delay profiles look qualitatively different for subsurface scattering and diffuse interreflections, which are short-range indirect light effects, versus specular interreflection that has long range. We note that Wu et al. performed a similar analysis using temporal delay for time-of-flight imaging [28].

In Fig. 9, we image a scene with a variety of these effects and show their delay profiles. Note how specular interreflections from the mirror ball (blue) have two peaks in their delay profile. This is due to a diffuse reflection from the page at $t_d = 0$ coupled with a peak from the specular reflection of the mirror ball. For the near corner of the book (red) and candle (yellow), their broadened delay profiles are due to subsurface scattering. The more translucent the object, the more broader its delay profile (see also milk results in Section 8). Note that the delay profiles are not symmetric around zero as one would expect, but are affected by the surface geometry/surface normal at those points. This relationship between symmetry and surface normal is a subject of further investigation.

Material Recognition of Subsurface Scattering. The use of delay and exposure can yield fundamental new information about light scattering in materials, particularly subsurface scattering. Previous researchers have used time-of-flight measurements to achieve a similar result [28], [57]. Consider
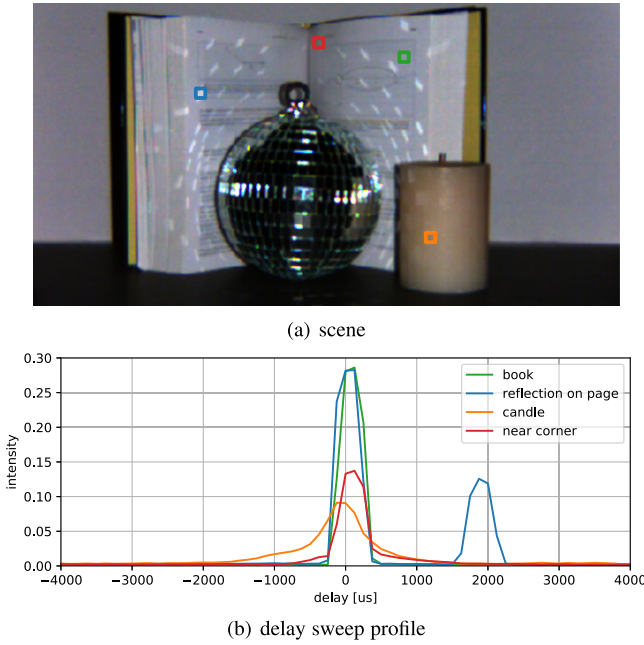
(a) scene

(b) delay sweep profile

Fig. 9. We perform a delay sweep of the scene shown in (a), and plot the delay profiles for selected pixels in the image (b). Note how subsurface scattering material like the candle has a wide broadening profile (orange), while diffuse interreflection in the near corner has a steeper profile (red). The diffuse reflection from the book page itself has an unimodal peak (green), but the specular interreflection has a bimodal peak (blue).

the delay profile for a given material. We expect the maximum of this plot to be at $t_d = 0$. However, our intuition is that the more subsurface scattering present in the material, the more spread out the delay profile will be.

In Fig. 10, we tested this hypothesis and its usefulness for material recognition of subsurface scattering in common household items. Using Episcan3D, we imaged containers of different material samples from above as shown in Fig. 10a. The materials we tested were three varieties of milk (fat free, 2 percent, and whole), toothpaste, and liquid soap. All of these items were white in color, and difficult to identify with RGB information alone. We plotted their average delay profiles for a set of their pixels shown in Fig. 10b. We normalized these delay profiles using the area under the curve to cancel out the effects of albedo.

Using training and test images, we trained a support vector machine (SVM) with nonlinear kernel (radial Gaussian basis function) to get a per-pixel semantic segmentation of the

materials (Fig. 10c) and a confusion matrix (Fig. 10d). We achieved over 90 percent recognition for all the materials. We note that the only errors occurred for pixels near the edge of the container, where possibly the scattering profile changes for the materials due to the asymmetry of a boundary condition. This is an interesting avenue of future research to use delay profiles to better model or inverse render subsurface scattering. This application is not meant for robust instance-level material recognition, but highlights the usefulness of delay profiles for understanding subsurface scattering in materials.

9 RESULTS: ILLUMINATION DEMULTIPLEXING

Sharpening Epipolar Imaging. In epipolar imaging, there is an inherent trade-off between the amount of non-epipolar or indirect light that leaks into the signal and exposure t_e. As noted earlier, a larger exposure value, typically $t_e > 500$ microseconds, will allow more short-range indirect light to be captured. This indirect component can be reduced by reducing or "tightening" the exposure to a smaller time, thus only exposing the epipolar row during capture. However, decreasing the exposure also increases overall noise in the images.

To solve this trade-off, we utilize our illumination demultiplexing algorithm to synthesize a "sharper" epipolar image that has the SNR of a large exposure, but reduced indirect component of a tight/short exposure. This is done by resolving light transport to a fine resolution in projector rows v in Equation (5). We can computationally render an epipolar image to the limit of the light's illumination width I_w.

In Fig. 11, we image a rose candle made of translucent wax. We synthesize in Fig. 11c a tighter epipolar image than a regular epipolar image with exposure $t_e = 600$ microseconds, shown in Fig. 11b. Note how the regular epipolar image cannot remove the subsurface scattering of the candle, but the sharpened epipolar image removes all these effects. Looking at the cross-section pixel values in Fig. 11d, the sharper epipolar image has more contrast amongst its rose petals. This sharpening has applications for when the system has a large exposure, and thus needs computation to generate a tighter epipolar image.

Relighting. In addition, 1D light transport allows us to synthesize novel images. For instance, we can render a new image with a novel illumination pattern of any linear combination of projector rows using the T operator. In Fig. 12, we synthesize relighting from a single line illumination for the

(a) Materials

(b) Delay profiles

(c) Classification Result
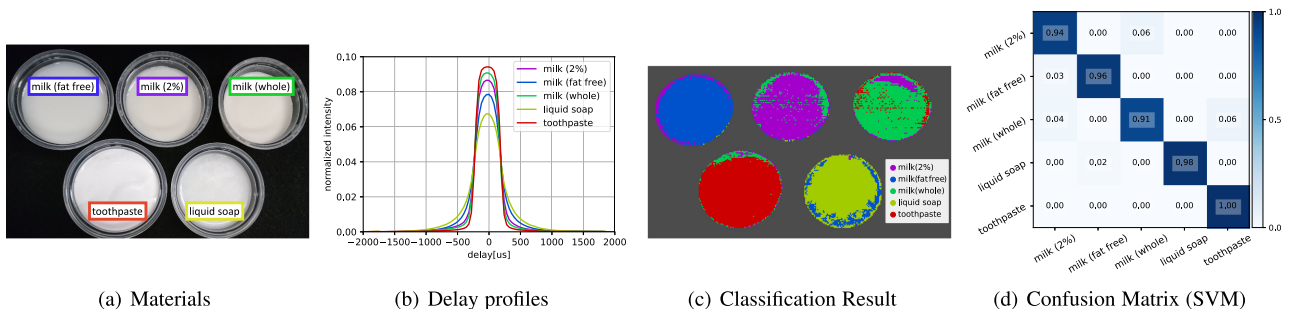

(d) Confusion Matrix (SVM)

Fig. 10. Using varying delay, we can perform recognition and analysis of subsurface scattering materials. In (a), fat free, 2 percent, whole milk, toothpaste, and liquid soap were imaged. Note that all materials are white in color, and difficult to distinguish visually. Their average pixel delay profiles are shown in (b). We use a nonlinear SVM to help perform semantic classification (c) and show the results of the confusion matrix (d). Note that all materials were correctly identified with most pixels semantically segmented correctly.
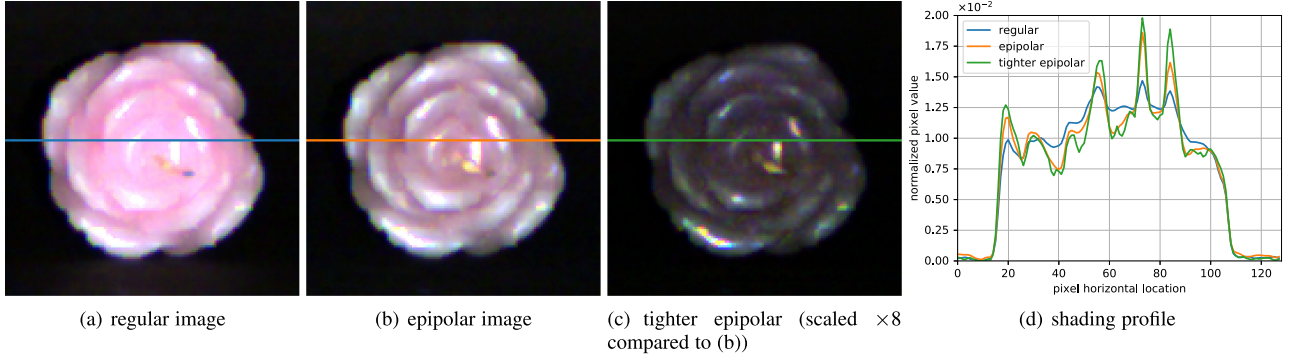
(a) regular image   (b) epipolar image   (c) tighter epipolar (scaled ×8 compared to (b))   (d) shading profile

Fig. 11. Imaging a wax rose candle in epipolar mode (b) with an exposure of $600 \ \mu s$ does not remove the subsurface scattering. Demultiplexing the image stack to recover 3D light transport, we synthesize a tighter epipolar image in (c) which preserves sharp features and highlights while removing the subsurface scattering from the epipolar image. In (d), we plot pixel values for a single scan line for comparison, note how the tighter epipolar image has larger contrast.

(a)   (b) Synthesized Result   (c) Actual single light projection at 16ms   (d) Actual single line projection at 800ms
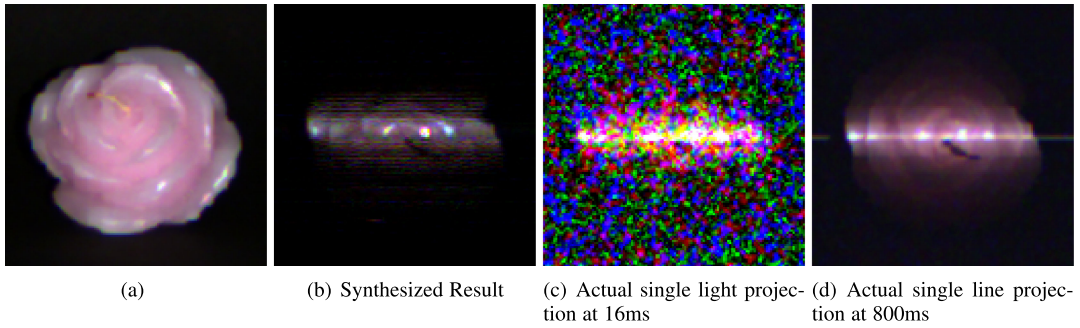
Fig. 12. Relighting under virtual single line illumination of a wax rose (a) Since the signal of the single line illumination is too weak, we brightened both synthesized (b) and actual observation (c) by an equal amount for visualization. Note that the synthesized result (b) has much better noise properties than an actual single line projection at exposure 16 ms (c). Our method achieves similar noise performance to (d) a 800 ms exposure, but is limited to short light transport effects due to our assumption of sparsity in optimization.

imaged rose. Please see the supplemental material, available online, for a video of this relighting effect.

For this single line relighting of the scene, we compare our method in Fig. 12b versus conventional imaging techniques. We show the comparison against a single projected line with exposure of 16 milliseconds in Fig. 12c, and a single line projection with exposure of 800 milliseconds in Fig. 12d. Note that our method achieves better noise performance than Fig. 12c since we utilize multiplexed illumination to capture our delay-exposure stack. Our method achieves similar performance to Fig. 12d in terms of noise, but requires multiple images and does not capture the long range light transport effects for far away rows due to the sparsity assumption in our optimization.

10 RESULTS: VISUALIZING BLOOD VESSELS THROUGH SKIN

For many biomedical and clinical applications, visible non-destructive imaging through skin to see blood vessels and structures is important. In particular, peripheral venous access for the basilic and cephalic vein in the inner arm is used for blood draws and intravenous drips. Visualizing these also helps with identification and diagnoses of symptoms such as varicose veins in patients. However, skin features strong subsurface scattering that reduces the contrast necessary to image these blood vessels. This is particularly

difficult for darker skin tones or dehydrated patients where signal is relatively low from scattering.

In addition, there is a need for low power and low cost imaging hardware to perform skin imaging. Many patients do not have access to a local hospital particularly in underdeveloped countries, and thus the imaging hardware needs to be portable, work out in the field under varying ambient illumination (e.g., in the sun). We argue that our projector-camera system with indirect imaging is well-suited to solve these issues for robust skin imaging. Note that a particularly compelling advantage of our method is that it can be performed in real-time, without the need for optimization or post-processing to perform vein visualization.

To image blood vessels embedded in the skin, we require capturing short-range indirect light that is the light scattered from a certain depth in the tissue. In our experiments, we utilize a delay of 400–600 microseconds, to capture images for a target that is approximately 0.5 meters away. In Fig. 16, we show the results for various different places on the body. To provide a reference for our results, we also show the images from a commercial medical imaging device known as Statvein. Statvein projects red and infrared light onto the target, and then overlays a visualization of the veins underneath onto the projection. We note that this is not a direct comparison as Statvein performs in-situ visualization, while our method presents the visualization on a separate screen.

(a) Indoor Environment   (b) Photo   (c) Direct   (d) Global   (e) Short-range Indirect (our method)   (f) Statvein

(g) Outdoor Environment   (h) Photo   (i) Direct   (j) Global   (k) Short-range Indirect (our method)
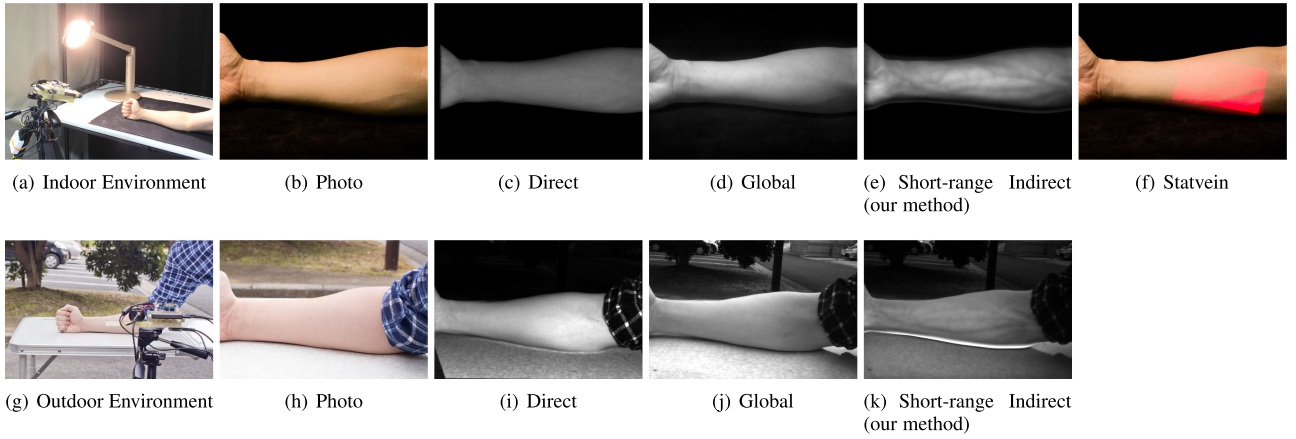
Fig. 13. Blood vessel visualization under strong ambient light both indoors (a) and outdoors (b). Note that the global component loses contrast and vessel structure due to ambient light in (d) and (j), yet the short-range indirect imaging maintains ambient light rejection to recover these vessels in (e) and (k).

In Fig. 16, we compared our method of capturing short-range indirect light using a specific delay versus several baselines including global light and Statvein. We tested against a variety of body parts including arm, elbow, face, and leg, as well as testing a lighter and darker skin tone. Note how short-range indirect imaging preserves more blood vessel structures than global or Statvein, and is even able to recover some blood vessels in the darker skin. This shows the energy-efficiency of this imaging method by only collecting photons along the desired light transport paths. Statvein uses re-projection to visualize blood vessels directly on the skin, and thus suffers from difficulty when there is a lot of hair or curvature present as in the outer arm for darker skin. Episcan3D using short-range indirect (delay) imaging can identify structures like the basilic and cephalic veins in the inner forearm, which corresponds to imaging *1-5* millimeters deep. We emphasize again that the indirect delay imaging can be captured and visualized in real-time, please refer to the supplemental material, available online, for videos. We also anticipate that if the light source was changed to infrared, we would see even deeper structures in human skin, or if the resolution of the camera was higher, we could visualize micro-vessels such as capillaries.

We also tested our method's robustness to strong ambient light. This is a common medical situation due to bright lights that are present for surgical procedures or bright sunlight for outdoor medical procedures in the field. We tested both these environments in Fig. 13. Here, we see that the contrast of global light is completely lost as it is overpowered by the ambient light, and Statvein can only identify major blood vessels in the arm. However short-range indirect imaging is robust to this ambient illumination, and still recovers finer blood vessel structure than any of the other methods. We believe these are promising results for this device for skin imaging in varying illumination conditions.

Contrast-Enhancement. We present an algorithm for a contrast-enhanced image computed in post-processing on a stack of varying delay images. Since different veins appear at different depths in the skin, we wish to fuse local spatial regions from different delay images to maximize the contrast displayed.

We first collect a sweep of delay images for the scene. To process, we take spatial regions or patches of size 200×200 at a time. We found that this patch size gave us the best results to measure local contrast. Each patch is then filtered using a bilateral filter [58] to enhance edge sharpness while reducing noise. Then for each patch, we calculate

$$t_d^*(s,t) = \underset{t_d}{\operatorname{argmax}} ||\nabla I_{t_d}||, \tag{7}$$

where $||\nabla I_{t_d}||$ is the gradient image of the patch for a given delay, and (s,t) is the coordinate for the pixel in the patch. Thus for each pixel, we get the delay t_d^* with the maximum local contrast, that preserves the image. We can compose these patches together to form a heat map of delay indices. As a final step, we blur this heat map to avoid sharp transitions in delay that results in image artifacts. The final contrast-enhanced image is formed by $I(s,t) = I_{t_d^*}(s,t)$. In Fig. 14, we can see the contrast enhancement using this algorithm versus capturing a single delay image alone.

Pulse Rate Extraction Using Motion Magnification. Regular, non-invasive monitoring of pulse rate and other vital signs has many clinical applications. We show that our method of indirect imaging for veins improves the extraction of pulse rate including a better signal-to-noise ratio. In previous work, researchers invented the technique of motion magnification to visualize subtle movements or changes in color at certain temporal frequencies [50], [59]. This algorithm uses a spatial pyramid for the image, and then applies a temporal filter to select a temporal signal per pixel to amplify. We use this algorithm to magnify the changes in indirect light due to blood flow. In Fig. 15a, you can see the extracted blood pulse from the short-range indirect light images. We recovered a blood pulse of 71.25 bpm approximately, while a ground truth heart rate monitor from the Xiaomi Mi Band 2 smartwatch measured 73 bpm. We also compared in Fig. 15b signals from a single pixel from a vein in the images with regular, direct, global, and indirect light as well as with no motion magnification. We used motion magnification using an ideal temporal filter with $f_{low} = 0.5$Hz and $f_{high} = 2$Hz, and a magnification factor $\alpha = 50$ and 4 pyramid levels for all our results. Further advanced motion magnification algorithms such as [60] could potentially yield

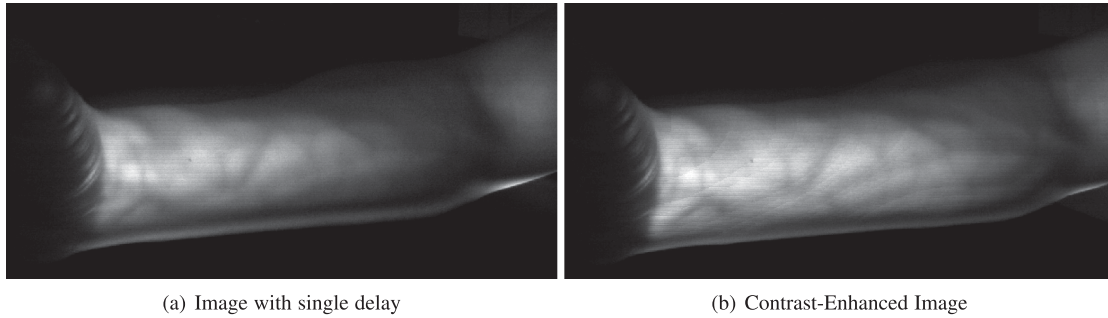(a) Image with single delay   (b) Contrast-Enhanced Image

Fig. 14. Using our contrast-enhancement algorithm, we are able to find a delay per local spatial region which maximizes the spatial contrast. This results in a enhanced blood vessel visualization (b) as compared to capturing a single delay image as in (a).

even more accurate results, which is an avenue of future work. Note how the indirect light has the most amplitude swing after motion magnification, and the blood pulse was calculated to 75 beats per minute. Please see the supplemental videos, available online, for visualizing the motion-magnified indirect light from the pulse.

11 DISCUSSION

We have presented a new imaging modality that exploits the 3D light transport between planar illumination and camera pixels. Using the observation that the synchronized rolling shutter of an epipolar projector-camera system performs illumination multiplexing, we formulate a forward imaging model for capturing images of varying delay and exposure. With these delay-exposure image stacks, we perform demultiplexing with a convex optimization algorithm to estimate 3D light transport.

Imaging using varying delay and exposure affords a compelling set of visual applications. Delay is particularly useful as it allows visualization of short and long-range indirect light, analysis of the characteristic type (subsurface scattering, specular and diffuse interreflection) using delay profiles, and helps with material recognition of visually indistinguishable materials by the shape of their subsurface scattering kernels. In addition, estimated 3D light transport from projector allows epipolar sharpening and relighting, giving a level of software control in the imaging process for post-capture editing.

The most exciting application from our perspective is the ability to see blood vessels in human skin with real-time capture and visualization. Our method is robust to strong ambient illumination, varying curvature of the target, obstructions such as hair on the skin, and works for even darker skin tones. Our Episcan3D prototype used for these results is approximately 20 cm × 15 cm, and can be easily used for portable monitoring of blood vessels deployed in the field.

Limitations. However, there are some limitations for the proposed imaging acquisition and algorithms in this paper. The demultiplexing algorithm is not real-time, requiring 80–100 images in the delay-exposure stack for acquisition, and taking several minutes to estimate the light transport. Further, this light transport is limited to 3D since our imaging model assumes projector illumination as impulse rows rather than the full 4D light transport. This affects our relighting to one-dimensional lighting directions. Of course, this limitation can be mitigated by utilizing spatial coding in the projector [31], but would increase the number of acquisition images and processing time.

In several of our applications, we are unable to capture short-range indirect light which is very near to the epipolar plane. This is due to synchronization effects such as laser jitter and alignment issues in the experimental prototype. This precise optical calibration limits the ability for the projector to be physically decoupled from the camera, preventing diverse viewpoints from either the projector or camera.

(a) Motion-magnified Pulse   (b) Comparison of light transport components
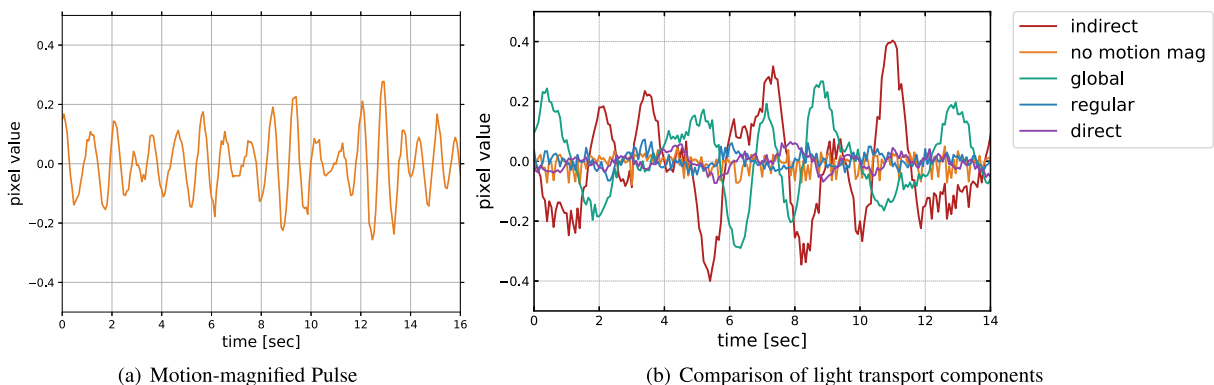
Fig. 15. Using motion magnification [50], we can extract the pulse from a single pixel on the vein of the arm in (a) from the short-range indirect light captured by Episcan3D. The approximate beats per minute extracted is 71.25 bpm, while the ground truth beats per minute measured using a Xiaomi Mi Band 2 smart-watch sensor is 73 bpm. In a different experiment (b), we plot the amplitudes for the signals for regular, direct, global, and indirect light as well as indirect light with no motion magnification. Note how only global and indirect light are able to recover pulse when motion magnified, and further indirect light has better SNR when magnified.
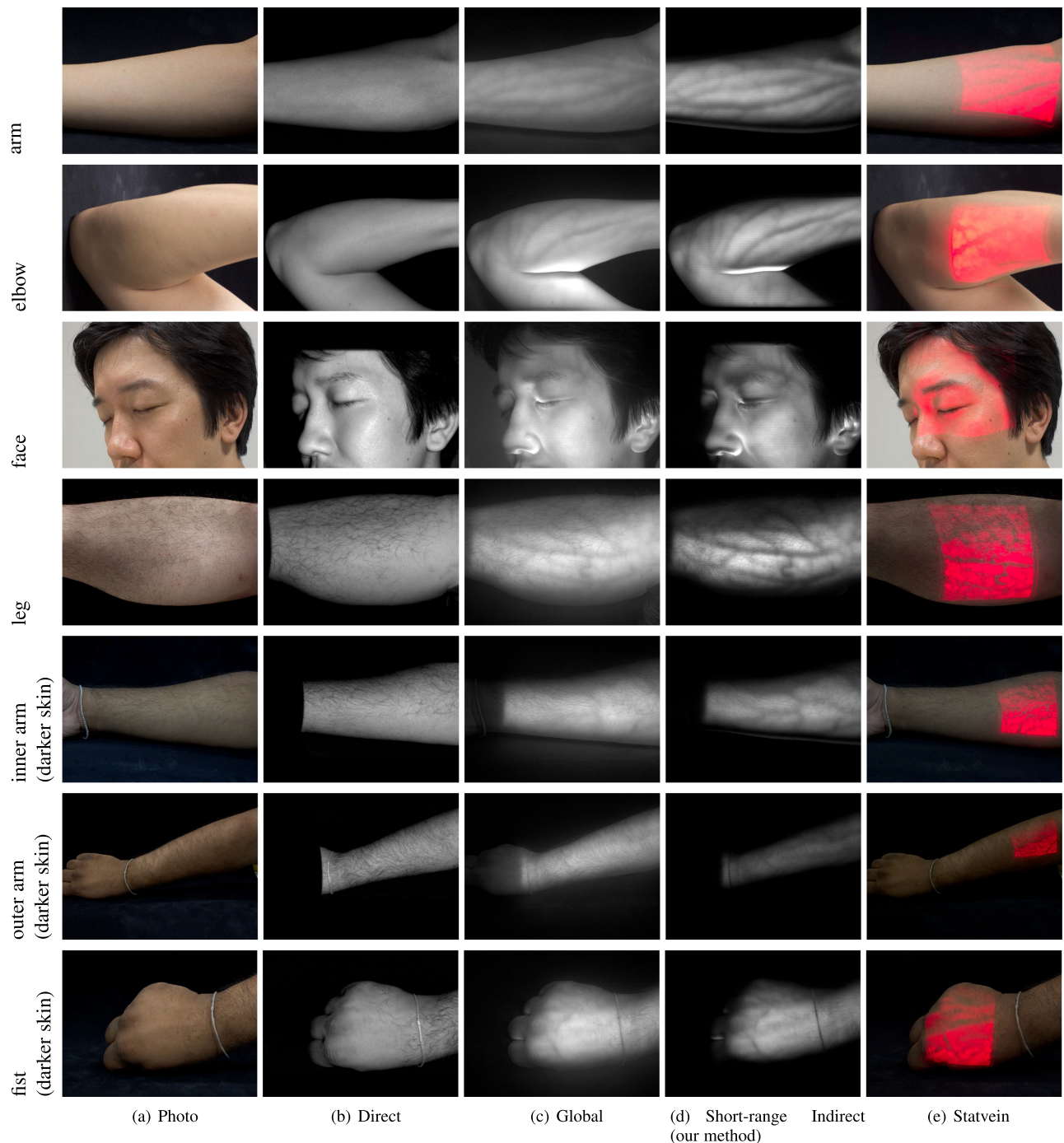
Fig. 16. Comparing visualizations for blood vessels for a variety of body parts and skin tones. Notice capturing short-range indirect light using delay imaging yields more vein structure than the direct component, and with higher contrast than the global component. We also note that it is robust to hair and darker skin as compared to Statvein, a commercial medical imaging device.

Future Work. One interesting avenue of future research is to identify the connection between delay defined in this paper and temporal delay related to time-of-flight imaging. Our delay clearly sets a lower bound on the time-of-flight, namely the minimum optical path length from two-bounce light (e.g., projector row i to scene point 1 to scene point 2 to camera pixel in row j). In principle, it may be possible to obtain the transient image of a scene if one can obtain accurate synchronization timings for the device. Our method can be extended to imaging systems where exposure is decoupled from delay/row-offset as in ROI systems like EpiTOF [3]. This would allow tighter isolation of key light transport components such as bands of indirect light at higher SNR. In addition, it would be useful to have control over the projector's raster scanning behavior, and estimate 4D light transport from this illumination. Such programmability has recently been shown to be useful for performing disparity gating and capturing complex geometric light transport paths [61], [62]. Parametric analysis of epipolar and non-epipolar light using delay and exposure and possibly other hardware mechanisms can lead to future insights into the physical nature of these visual effects. We hope that our research shows a path forward for

temporal synchronization between projectors and cameras to selectively capture many different components of light transport.

ACKNOWLEDGMENTS

REFERENCES

[1] M. Gupta, A. Agrawal, A. Veeraraghavan, and S. G. Narasimhan, "Structured light 3D scanning in the presence of global illumination," in *Proc. IEEE Conf. Comput. Vis. Pattern Recognit.*, 2011, pp. 713–720.

[2] S. K. Nayar, K. Ikeuchi, and T. Kanade, "Shape from interreflections," *Int. J. Comput. Vis.*, vol. 6, no. 3, pp. 173–195, 1991.

[3] S. Achar, J. R. Bartels, W. L. Whittaker, K. N. Kutulakos, and S. G. Narasimhan, "Epipolar time-of-flight imaging," *ACM Trans. Graphics*, vol. 36, no. 4, 2017, Art. no. 37.

[4] H. W. Jensen, S. R. Marschner, M. Levoy, and P. Hanrahan, "A practical model for subsurface light transport," in *Proc. 28th Annu. Conf. Comput. Graphics Interactive Techn.*, 2001, pp. 511–518.

[5] C.-Y. Tsai, K. N. Kutulakos, S. G. Narasimhan, and A. C. Sankaranarayanan, "The geometry of first-returning photons for non-line-of-sight imaging," in *Proc. IEEE Int. Conf. Comput. Vis. Pattern Recognit.*, 2017, pp. 2336–2344.

[6] S. K. Nayar, G. Krishnan, M. D. Grossberg, and R. Raskar, "Fast separation of direct and global components of a scene using high frequency illumination," *ACM Trans. Graphics*, vol. 25, no. 3, pp. 935–944, 2006.

[7] M. O'Toole, R. Raskar, and K. N. Kutulakos, "Primal-dual coding to probe light transport," *ACM Trans. Graphics*, vol. 31, no. 4, 2012, Art. no. 39.

[8] M. O'Toole, S. Achar, S. G. Narasimhan, and K. N. Kutulakos, "Homogeneous codes for energy-efficient illumination and imaging," *ACM Trans. Graphics*, vol. 34, no. 4, 2015, Art. no. 35.

[9] M. O'Toole, J. Mather, and K. N. Kutulakos, "3D shape and indirect appearance by structured light transport," in *Proc. IEEE Conf. Comput. Vis. Pattern Recognit.*, 2014, pp. 3246–3253.

[10] H. Kubo, S. Jayasuriya, T. Iwaguchi, T. Funatomi, Y. Mukaigawa, and S. G. Narasimhan, "Acquiring and characterizing planeto-ray indirect light transport," in *Proc. IEEE Int. Conf. Comput. Photography*, 2018, pp. 1–10.

[11] P. Debevec, T. Hawkins, C. Tchou, H.-P. Duiker, W. Sarokin, and M. Sagar, "Acquiring the reflectance field of a human face," in *Proc. 27th Annu. Conf. Comput. Graphics Interactive Techn.*, 2000, pp. 145–156.

[12] C. M. Goral, K. E. Torrance, D. P. Greenberg, and B. Battaile, "Modeling the interaction of light between diffuse surfaces," *ACM SIGGRAPH Comput. Graphics*, vol. 18, no. 3, pp. 213–222, 1984.

[13] R. Ng, R. Ramamoorthi, and P. Hanrahan, "All-frequency shadows using non-linear wavelet lighting approximation," *ACM Trans. Graphics*, vol. 22, no. 3, pp. 376–381, 2003.

[14] P. Peers, D. K. Mahajan, B. Lamond, A. Ghosh, W. Matusik, R. Ramamoorthi, and P. Debevec, "Compressive light transport sensing," *ACM Trans. Graphics*, vol. 28, no. 1, 2009, Art. no. 3.

[15] P. Sen and S. Darabi, "Compressive dual photography," *Comput. Graphics Forum*, vol. 28, no. 2, pp. 609–618, 2009.

[16] G. Garg, E.-V. Talvala, M. Levoy, and H. P. Lensch, "Symmetric photography: Exploiting data-sparseness in reflectance fields," in *Proc. 17th Eurographics Conf. Rendering Techn.*, 2006, pp. 251–262.

[17] M. O'Toole and K. N. Kutulakos, "Optical computing for fast light transport analysis," *ACM Trans. Graphics*, vol. 29, no. 6, 2010, Art. no. 164.

[18] S. M. Seitz, Y. Matsushita, and K. N. Kutulakos, "A theory of inverse light transport," in *Proc. IEEE Int. Conf. Comput. Vis.*, 2005, pp. 1440–1447.

[19] J. Bai, M. Chandraker, T.-T. Ng, and R. Ramamoorthi, "A dual theory of inverse and forward light transport," in *Proc. Eur. Conf. Comput. Vis.*, 2010, pp. 294–307.

[20] S. Achar, S. T. Nuske, and S. G. Narasimhan, "Compensating for motion during direct-global separation," in *Proc. IEEE Int. Conf. Comput. Vis.*, 2013, pp. 1481–1488.

[21] J. Gu, T. Kobayashi, M. Gupta, and S. K. Nayar, "Multiplexed illumination for scene recovery in the presence of global illumination," in *Proc. IEEE Int. Conf. Comput. Vis.*, 2011, pp. 691–698.

[22] D. Reddy, R. Ramamoorthi, and B. Curless, "Frequency-space decomposition and acquisition of light transport under spatially varying illumination," in *Proc. Eur. Conf. Comput. Vis.*, 2012, pp. 596–610.

[23] S. Lin, Y. Li, S. B. Kang, X. Tong, and H.-Y. Shum, "Diffuse-specular separation and depth recovery from image sequences," in *Proc. Eur. Conf. Comput. Vis.*, 2002, pp. 210–224.

[24] W.-C. Ma, T. Hawkins, P. Peers, C.-F. Chabert, M. Weiss, and P. Debevec, "Rapid acquisition of specular and diffuse normal maps from polarized spherical gradient illumination," in *Proc. 18th Eurographics Conf. Rendering Techn.*, 2007, pp. 183–194.

[25] S. K. Nayar, X.-S. Fang, and T. Boult, "Separation of reflection components using color and polarization," *Int. J. Comput. Vis.*, vol. 21, no. 3, pp. 163–186, 1997.

[26] S. Umeyama and G. Godin, "Separation of diffuse and specular components of surface reflection by use of polarization and statistical analysis of images," *IEEE Trans. Pattern Anal. Mach. Intell.*, vol. 26, no. 5, pp. 639–647, May 2004.

[27] B. Dong, Y. Dong, X. Tong, and P. Peers, "Measurement-based editing of diffuse albedo with consistent interreflections," *ACM Trans. Graphics*, vol. 34, no. 4, pp. 112:1–112:11, Jul. 2015.

[28] D. Wu et al., "Decomposing global light transport using time of flight imaging," *Int. J. Comput. Vis.*, vol. 107, no. 2, pp. 123–138, 2014.

[29] Y. Y. Schechner, S. K. Nayar, and P. N. Belhumeur, "Multiplexing for optimal lighting," *IEEE Trans. Pattern Anal. Mach. Intell.*, vol. 29, no. 8, pp. 1339–1354, Aug. 2007.

[30] N. Ratner and Y. Y. Schechner, "Illumination multiplexing within fundamental limits," in *Proc. IEEE Conf. Comput. Vis. Pattern Recognit.*, Jun. 2007, pp. 1–8.

[31] P. Sen, B. Chen, G. Garg, S. R. Marschner, M. Horowitz, M. Levoy, and H. Lensch, "Dual photography," *ACM Trans. Graphics*, vol. 24, no. 3, pp. 745–755, 2005.

[32] R. Raskar, A. Agrawal, J. Tumblin, R. Raskar, A. Agrawal, and J. Tumblin, "Coded exposure photography," *ACM Trans. Graphics*, vol. 25, no. 3, Jul. 2006, Art. no. 795. [Online]. Available: http://portal.acm.org/citation.cfm?doid=1141911.1141957

[33] Y. Hitomi, J. Gu, M. Gupta, T. Mitsunaga, and S. K. Nayar, "Video from a single coded exposure photograph using a learned overcomplete dictionary," in *Proc. IEEE Int. Conf. Comput. Vis.*, 2011, pp. 287–294.

[34] J. Gu, Y. Hitomi, T. Mitsunaga, and S. Nayar, "Coded rolling shutter photography: Flexible space-time sampling," in *Proc. IEEE Int. Conf. Comput. Photography*, 2010, pp. 1–8.

[35] M. Gupta, A. Agrawal, A. Veeraraghavan, and S. G. Narasimhan, "Flexible voxels for motion-aware videography," in *Proc. Eur. Conf. Comput. Vis.*, 2010, pp. 100–114.

[36] T. Hawkins, J. Cohen, C. Tchou, and P. Debevec, "Light Stage 2.0," in *Proc. SIGGRAPH Tech. Sketches*, 2001, Art. no. 217.

[37] P. Debevec, A. Wenger, C. Tchou, A. Gardner, J. Waese, and T. Hawkins, "A lighting reproduction approach to live-action compositing," in *Proc. 29th Annu. Conf. Comput. Graphics Interactive Techn.*, Jul. 2002, pp. 547–556.

[38] A. Wenger, A. Gardner, C. Tchou, J. Unger, T. Hawkins, and P. Debevec, "Performance relighting and reflectance transformation with time-multiplexed illumination," *ACM Trans. Graphics*, vol. 24, no. 3, pp. 756–764, 2005.

[39] P. Einarsson et al., "Relighting human locomotion with flowed reflectance fields," in *Proc. 17th Eurographics Conf. Rendering Techn.*, 2006, pp. 183–194.

[40] M. Goesele, H. P. A. Lensch, J. Lang, C. Fuchs, and H.-P. Seidel, "DISCO: Acquisition of translucent objects," *ACM Trans. Graphics*, vol. 23, no. 3, pp. 835–844, Aug. 2004. [Online]. Available: http://doi.acm.org/10.1145/1015706.1015807

[41] S. J. Koppal, S. Yamazaki, and S. G. Narasimhan, "Exploiting DLP illumination dithering for reconstruction and photography of high-speed scenes," *Int. J. Comput. Vis.*, vol. 96, no. 1, pp. 125–144, 2012.

[42] V. P. Zharov, S. Ferguson, J. F. Eidt, P. C. Howard, L. M. Fink, and M. Waner, "Infrared imaging of subcutaneous veins," *Lasers Surgery Med.: Official J. Amer. Soc. Laser Med. Surgery*, vol. 34, no. 1, pp. 56–61, 2004.

[43] A. Fercher and J. D. Briers, "Flow visualization by means of single-exposure speckle photography," *Opt. Commun.*, vol. 37, no. 5, pp. 326–330, 1981.

[44] P. Goedhart, M. Khalilzada, R. Bezemer, J. Merza, and C. Ince, "Sidestream dark field (SDF) imaging: A novel stroboscopic LED ring-based imaging modality for clinical assessment of the microcirculation," *Opt. Exp.*, vol. 15, no. 23, pp. 15 101–15 114, 2007.

[45] A. Kadambi, H. Ikoma, X. Lin, G. Wetzstein, and R. Raskar, "Subsurface enhancement through sparse representations of multispectral direct/global decomposition," in *Proc. Comput. Opt. Sens. Imag.*, 2013.

[46] G. Satat, C. Barsi, and R. Raskar, "Skin perfusion photography," in *Proc. IEEE Int. Conf. Comput. Photography*, 2014, pp. 1–8.

[47] A. Ghosh, T. Hawkins, P. Peers, S. Frederiksen, and P. Debevec, "Practical modeling and acquisition of layered facial reflectance," *ACM Trans. Graphics*, vol. 27, no. 5, pp. 139:1–139:10, Dec. 2008.

[48] W. Verkruysse, L. O. Svaasand, and J. S. Nelson, "Remote plethysmographic imaging using ambient light," *Opt. Exp.*, vol. 16, no. 26, pp. 21 434–21 445, 2008.

[49] M. Kumar, A. Veeraraghavan, and A. Sabharwal, "DistancePPG: Robust non-contact vital signs monitoring using a camera," *Biomed. Opt. Exp.*, vol. 6, no. 5, pp. 1565–1588, 2015.

[50] C. Liu, A. Torralba, W. T. Freeman, F. Durand, and E. H. Adelson, "Motion magnification," *ACM Trans. Graphics*, vol. 24, no. 3, pp. 519–526, 2005.

[51] S. Diamond and S. Boyd, "CVXPY: A python-embedded modeling language for convex optimization," *J. Mach. Learn. Res.*, vol. 17, no. 1, pp. 2909–2913, 2016.

[52] P. Hanrahan and W. Krueger, "Reflection from layered surfaces due to subsurface scattering," in *Proc. 20th Annu. Conf. Comput. Graphics Interactive Techn.*, 1993, pp. 165–174.

[53] J. Wenzel, "Mitsuba renderer," 2010. [Online]. Available: http://www.mitsuba-renderer.org/

[54] J. R. Frisvad, T. Hachisuka, and T. K. Kjeldsen, "Directional dipole model for subsurface scattering," *ACM Trans. Graphics*, vol. 34, no. 1, pp. 5:1–5:12, Dec. 2014.

[55] R. Habel, P. H. Christensen, and W. Jarosz, "Photon beam diffusion: A hybrid monte carlo method for subsurface scattering," in *Proc. Eurographics Symp. Rendering*, 2013, pp. 27–37.

[56] S. G. Narasimhan, M. Gupta, C. Donner, R. Ramamoorthi, S. K. Nayar, and H. W. Jensen, "Acquiring scattering properties of participating media by dilution," *ACM Trans. Graphics*, vol. 25, no. 3, pp. 1003–1012, 2006.

[57] S. Su et al., "Material classification using raw time-of-flight measurements," in *Proc. IEEE Conf. Comput. Vis. Pattern Recognit.*, 2016, pp. 3503–3511.

[58] C. Tomasi and R. Manduchi, "Bilateral filtering for gray and color images," in *Proc. 6th Int. Conf. Comput. Vis.*, 1998, pp. 839–846.

[59] H.-Y. Wu, M. Rubinstein, E. Shih, J. Guttag, F. Durand, and W. T. Freeman, "Eulerian video magnification for revealing subtle changes in the world," *ACM Trans. Graphics*, vol. 31, no. 4, 2012, Art. no. 65.

[60] N. Wadhwa, M. Rubinstein, F. Durand, and W. T. Freeman, "Phase-based video motion processing," *ACM Trans. Graphics*, vol. 32, no. 4, 2013, Art. no. 80.

[61] J. Wang, J. Bartels, W. Whittaker, A. Sankaranarayanan, and S. Narasimhan, "Programmable triangulation light curtains," in *Proc. Eur. Conf. Comput. Vis.*, 2018, pp. 20–35.

[62] T. Ueda, H. Kubo, S. Jayasuriya, T. Funatomi, and Y. Mukaigawa, "Slope disparity gating using a synchronized projector-camera system," in *Proc. IEEE Int. Conf. Comput. Photography*, 2019, pp. 1–9.

Hiroyuki Kubo received the MS and PhD degrees from Waseda University, Japan, in 2008 and 2012, respectively. He has been an assistant professor with the Nara Institute of Science and Technology (NAIST), Japan since 2014. He was a visiting scholar with Carnegie Mellon University, in 2017. He was a researcher with Canon Inc. in 2012-2014.

Suren Jayasuriya received the BS degree in mathematics and the BA degree in philosophy from the University of Pittsburgh, Pennsylvania, PA, United States in 2012, and the PhD degree in electrical and computer engineering from Cornell University, in 2017. He has been an assistant professor with Arizona State University (ASU) since 2018. He was a postdoctoral fellow with the Robotics Institute, Carnegie Mellon University, in 2017. His research interests include computational photography and imaging, computer vision, and image sensors. He is a member of the IEEE.

Takafumi Iwaguchi received the ME and PhD degrees from the Nara Institute of Science and Technology (NAIST), Japan, in 2016 and 2019, respectively. He has been an assistant professor with the Graduate School and Faculty of Information Science and Electrical Engineering, Kyushu University, Japan, since 2019. His research interests include computer vision, especially in light transport analysis and computational photography.

Takuya Funatomi received the BS degree in engineering, and the MS and PhD degrees in informatics from the Graduate School of Informatics, Kyoto University, Japan, in 2002, 2004, and 2007, respectively. He has been an associate professor with the Nara Institute of Science and Technology (NAIST), Japan, since 2015. He was an assistant professor with Kyoto University, Japan from 2007 to 2015, and a visiting assistant professor with Stanford University, in 2014. He has been working on 3D shape reconstruction of human as a deformable object and image processing techniques to observe human activity such as cooking. His research interests include computer vision, computer graphics, and pattern recognition. He is a member of the ACM, the IEEE Computer Society, the IEEE Communication Society, and the Institute of Electronics, Information and Communication Engineers of Japan.

Yasuhiro Mukaigawa received the ME and PhD degrees from the University of Tsukuba, Japan, in 1994 and 1997, respectively. He became a research associate with Okayama University, in 1997, an assistant professor with the University of Tsukuba, in 2003, an associate professor with Osaka University, in 2004, and a professor with the Nara Institute of Science and Technology (NAIST), in 2014. His current research interests include photometric analysis and computational photography. He is a member of the IEEE.

Srinivasa G. Narasimhan received the PhD degree from Columbia University, New York, NY, United States in December 2003. He is a professor of robotics and ECE (courtesy) with Carnegie Mellon University. His group focuses on novel techniques for imaging, illumination, and light transport to enable applications in vision, graphics, robotics, agriculture, and medical imaging. His works have received several awards: Best Demo Award (IEEE ICCP 2015), A9 Best Demo Award (IEEE CVPR 2015), Marr Prize Honorable Mention Award (2013), FORD URP Award (2013), Best Paper Runner up Prize (ACM I3D 2013), Best Paper Honorable Mention Award (IEEE ICCP 2012), Best Paper Award (IEEE PROCAMS 2009), the Okawa Research Grant (2009), the NSF CAREER Award (2007), the Adobe Best Paper Award (IEEE Workshop on Physics based methods in computer vision, ICCV 2007) and the IEEE Best Paper Honorable Mention Award (IEEE CVPR 2000). His research has been covered in popular press including *NY Times*, BBC, *PC magazine,* and *IEEE Spectrum* and is highlighted by NSF and NAE. He is the co-inventor of programmable headlights, Aqualux 3D display, Assorted-pixels, Motion-aware cameras, Episcan3D, EpiToF3D, and programmable triangulation light curtains. He co-chaired the International Symposium on Volumetric Scattering in Vision and Graphics in 2007, the IEEE Workshop on Projector-Camera Systems (PROCAMS) in 2010, and the IEEE International Conference on Computational Photography (ICCP) in 2011, co-edited a special journal issue on computational photography, and serves on the editorial board of the *International Journal of Computer Vision* and as area chair of top computer vision conferences (CVPR, ICCV, ECCV, BMVC, ACCV). He is a senior member of the IEEE.

▷ **For more information on this or any other computing topic, please visit our Digital Library at** www.computer.org/csdl.